

Convolutional neural network model for discrimination of harmful algal bloom (HAB) from non-HABs using Sentinel-3 OLCI imagery

Jisun Shin ^a, Boo-Keun Khim ^a, Lee-Hyun Jang ^b, Jinwook Lim ^b, Young-Heon Jo ^{a,*}

^a BK21 School of Earth and Environmental Systems, Pusan National University, 2, Busandaehak-ro 63 beon-gil, Geumjeong-gu, Busan 46241, Republic of Korea

^b LIONPLUS Corp., 38, Jungang-daero 1367 beon-gil, Dongnae-gu, Busan 47728, Republic of Korea

ARTICLE INFO

Keywords:

Magelefidinium polykrikoides

Alexandrium sp.

Sentinel-3 OLCI

Convolutional neural network

ABSTRACT

Harmful algal bloom (HAB) caused by *Magelefidinium polykrikoides* becomes frequent in Korean coastal waters during the mid-1990s and is now annual events on the southern coast of Korea. HAB often leads to high rates of fish mortality and subsequent economic losses in aquaculture. In addition, non-harmful algal blooms (non-HABs) caused by the dinoflagellate *Alexandrium* sp., *Mesodinium rubrum*, and the diatom *Skeletonema* sp. occur simultaneously in time and space. Because HAB and non-HABs are difficult to discriminate using multi-band satellite data, most previous studies have attempted only detection or qualitative classification with limited data. In contrast, in this current study, we aimed to quantitatively discriminate *M. polykrikoides* bloom associated HAB from non-HABs around the southern coast of Korea using a convolutional neural network (CNN) model with Sentinel-3 Ocean and Land Colour Instrument (OLCI) imagery with a spatial resolution of 300 m and 16 spectral bands for the first time. To identify the effect of non-HAB patches on the performance of the CNN model, five CNN models were trained with OLCI images as input and ground-truth HAB maps as output data. The appropriate figure-of-merits values (FOMs) with sensitivity of 0.53, precision of 0.92, and F-measure of 0.67 were reasonable when the CNN model trained using the dataset with the highest ratio of non-HABs patches was applied to HAB images. Even when non-HAB images were applied to the models, the CNN model exhibited the lowest error pixel count. Therefore, we confirmed that the CNN model, which can discriminate red tide blooms with subtle differences between the spectrum bands and spatial characteristics, helps solve the complexity and ambiguity in discriminating HAB from non-HABs.

1. Introduction

Magelefidinium polykrikoides is a red tide species that has caused Harmful algal bloom (HAB) in Korean coastal waters every year since the mid-1990s (Jeong and Kang, 2013; Lee et al., 2013); HAB is generally characterized by a large spatial extent (tens to hundreds of kilometers). Contact with *M. polykrikoides* bloom water (with cell density of > 1000 cells mL⁻¹) leads to rapid mortality in fish within hours and in shellfish within days (Gobler et al., 2008; Park et al., 2013; Tang and Gobler, 2009; Whyte et al., 2001). This large-scale mortality in finfish causes substantial economic losses. They occur frequently at Goheung, Yeosu, Namhae and Tongyeong on the southern coast of Korea (Fig. 1), mostly during summer, starting from mid-July to early September and lasting until the end of October. Red tide blooms caused by the dinoflagellate *Alexandrium* sp., *Chattonella* sp., and *Mesodinium rubrum* also occur at similar times and locations as *M. polykrikoides* bloom. Blooms

caused by diatoms, such as *Skeletonema* sp., are like other red tide blooms; there is considerable interspecies competition with dinoflagellate blooms. While high-density blooms caused by these red tide species may adversely affect marine ecosystem due to oxygen depletion, these blooms do not have a harmful effect on the surrounding environment and are thus referred to as non-harmful algal blooms (non-HABs). HAB and non-HABs may occur alone; however, they more often occur in a mixed state. Therefore, for an immediate and efficient response to HAB, it is essential to discriminate them from non-HABs.

The National Institute of Fisheries Science (NIFS), Republic of Korea, has monitored red tides since 1996 (NIFS, 2015). The institute provides daily red tide reports based on field measurements and cell densities that include causative organisms, affected and at-risk areas, and predictions for the development and spread of red tides. The NIFS provides red tide warning system fishermen and aquaculturists based on four levels: red tide emergence attention, red tide attention, red tide alert, and warning

* Corresponding author.

E-mail address: joyoung@pusan.ac.kr (Y.-H. Jo).

lift. For each level, criteria are set for the cell size and toxicity of dinoflagellate and diatom. Red tide warning systems have been issued based on *M. polykrikoides* blooms due to their harmful properties. In the event of *M. polykrikoides* blooms, information on these blooms is mixed with other red tide blooms that occur simultaneously. Therefore, information on non-HABs is occasionally included in daily red tide reports. Thus, it is difficult to obtain information on non-HABs alone. In fact, the only way for this information is currently through field sampling at discrete locations from research vessels. Hence, wide or detailed spatial and temporal distributions of red tide blooms cannot be provided. Remote sensing observation based on spectral information has the potential to compensate for these limitations of sparse field measurements.

Discriminating red tide blooms using the absorption properties of phytoplankton (measurable in a laboratory environment) has been attempted. Absorption properties vary depending on the type of pigment and cell size of phytoplankton (Bidigare et al., 1990; Ciotti et al., 2002; Nair et al., 2008; Shang et al., 2014). Thus, measuring the differences in the auxiliary absorption wavelength bands enables phytoplankton species to be identified. Although backscattering coefficient of phytoplankton is much smaller than the absorption coefficient; it is an important optical property that can distinguish red tide species. Cannizzaro et al. (2008) presented a classification technique to differentiate *K. brevis* blooms from other blooms using a bio-optical dataset consisting of remote-sensing reflectance (R_{rs}), absorption, backscattering, and chlorophyll (CHL) concentration. Ahn et al. (2009) reported that the shape, absorption, and scattering coefficients vary according to the red tide species. They reported that red tide species had main absorption peaks at wavelengths of 440 and 680 nm but subsidiary peaks at 460, 530, and 590 nm that differed slightly by species. They classified 8 red tide species among 21 species using these optical properties. Tao et al. (2015) compared the absorption and backscattering spectra of *Procentrum donghaiense* and diatoms and identified bloom waters by their low $R_{rs,555}$ and high band ratios of $R_{rs,555}/R_{rs,531}$. Kim et al. (2016) investigated the possibility of optically discriminating red tide blooms by focusing on *M. polykrikoides*. They generated a dataset of simulated remote sensing reflectance (R_{rs}) spectra using the Hydrolight software and bio-optical data. They proposed two R_{rs} band ratios $R_{rs,555}/R_{rs,531}$ and $R_{rs,488}/R_{rs,443}$ for discriminating high-density *M. polykrikoides* blooms. However, these optical features are difficult to apply to multispectral satellite data because of the lack of low spectral resolution and the small number of wavelength bands. In addition, these studies have limitations in the discrimination of red tide species in real complex marine environments due to the difficulty of culturing red tide species, the ambiguity of the distinction between similar species, and the

differences between cultivation environments and real marine environments.

Several studies have been conducted to detect red tide blooms using data from ocean color sensors, such as data from MODerate resolution Imaging Spectroradiometer (MODIS), Visible Infrared Imager Radiometer Suite (VIIRS), Geostationary Ocean Color Imager (GOCI), and Ocean and Land Colour Instrument (OLCI) (Hu et al., 2015; Izadi et al., 2021; Lee et al., 2020; Lou and Hu, 2014; Qi et al., 2015; Rodríguez-Benito et al., 2020; Shin et al., 2019; Son et al., 2012). Terrestrial sensors with high spatial resolution were used for the detection of red tide blooms (Liu et al., 2022; Shin et al., 2019; Shin et al., 2021). These past studies focused on true and false red tide blooms rather than classifying them, even detecting mixed red tide blooms as a single bloom. However, some studies have attempted to differentiate red tide species associated with specific blooms using satellite data. Sathyendranath et al. (2004) and Westberry et al. (2005) revealed multi-spectral patterns for the detection of diatom and the cyanobacterium *Trichodesmium spp.* based on semi-analytical models. Tao et al. (2015) developed a novel method for discriminating *P. donghaiense* from diatom blooms in the East China Sea using MODIS data based on the optical properties of blooms. Ghanea et al. (2016) developed a Hybrid Ocean colour Index (HOCl) to distinguish *Trichodesmium erythraeum* and *M. polykrikoides* from other red tide species in the Persian Gulf using MODIS data. Shin et al. (2017) proposed that red tide species which occur frequently in Korean coastal waters could be divided into two groups according to their CHL contents; they developed a system for red tide surveillance using GOCI images. Ghatkar et al. (2019) classified three major algal blooms, including *Trichodesmium erythraeum*, *Noctiluca scintillans*, and *M. polykrikoides* blooms, from remote sensing data using an extreme gradient-boosted decision tree model. Feng et al. (2020) developed a method based on backscattering for discriminating summer blooms of harmful raphidophytes (*Chattonella sp.*) and the diatom (*Skeletonema sp.*) using MODIS images in the Ariake Sea, Japan.

Until now, due to the difficulties of image collections related to various red tide blooms and the ambiguity of spectral distinction between red tide blooms in the satellite imagery, studies have only attempted to discriminate red tide blooms qualitatively using satellite data. Therefore, methods based on existing red tide indexes have limitations in discriminating red tide blooms. To overcome these limitations, deep learning approaches can be effective. Recently, convolutional neural network (CNN) model, which can resolve a problem of non-linear relationship between spectrum of red tide blooms, have been used for red tide detection. CNN model is an essential tool for deep learning and is particularly suited for image recognition (Yamashita et al., 2018). Kim

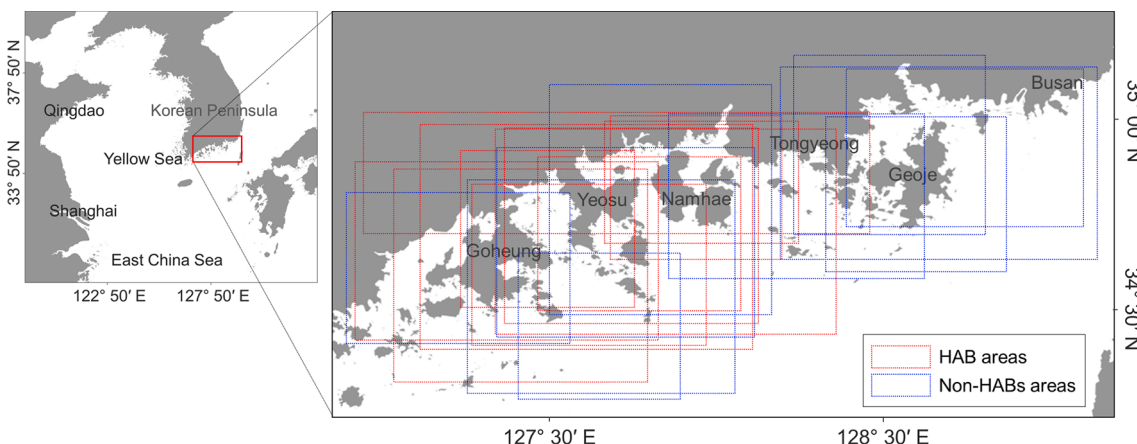


Fig. 1. Study area for discriminating harmful algal bloom (HAB) (the dotted red boxes) and non-HABs areas (the dotted blue boxes). HAB areas means that only *Margalefidinium polykrikoides* bloom occurred; non-HABs areas means that blooms are caused by a total of six red tide species, including *Alexandrium sp.*, *Chattonella sp.*, *Skeletonema sp.*, *Ceratium furca*, *Mesodinium rubrum*, and *Akashiwo sanguinea*. (For interpretation of the references to color in this figure legend, the reader is referred to the web version of this article.)

et al. (2019) proposed the automatic pixel-based detection of three red tide groups using a deep CNN model, U-Net, from GOCI images of the coast of the Korean Peninsula. The predicted red tide bloom maps showed considerable matching distribution of the three groups to the ground truths. Shin et al. (2021) developed a U-Net deep learning model for detecting *M. polykrikoides* blooms off the southern coast of Korea from PlanetScope imagery. The predicted map derived from U-Net provided reasonable red tide patterns for all water areas. However, no studies have attempted to discriminate *M. polykrikoides* blooms from other red tide blooms using a CNN model.

In this study, we aimed to quantitatively discriminate *M. polykrikoides* bloom from various red tide blooms along the southern coast of Korea. For this purpose, we visually inspected various red tide blooms using Sentinel-3 OLCI with a spatial resolution of 300 m and 16 spectral bands and investigated the OLCI-based spectral characteristics of HAB and non-HABs. We trained and tested a simple CNN model to discriminate between HAB and non-HABs. Finally, we qualitatively and quantitatively validated the CNN models using OLCI images.

2. Materials and methods

2.1. Study area

The study area covers the southern coast of South Korea. The area has two distinct zones: offshore zones, characterized by clear seawater due to the Kuroshio Current, and coastal zones, characterized by complex water properties due to high levels of colored dissolved organic matter and suspended sediment near the coast (Yoon et al., 2004; Son et al., 2012). Fig. 1 shows the known HAB and non-HAB areas of the study area. Red tide blooms mainly occur from Goheung to Tongyeong (NIFS, 2015) and extend into the East Sea of Korea. Non-HABs sometimes occurs alone, but mainly occurs in combination with HAB. In this study, only images with non-HABs occurred alone were selected.

2.2. Image processing

In this study, we used the OLCI imagery onboard Sentinel-3A and 3B (Donlon et al., 2012). The OLCI images around the Korean Peninsula

with a spatial resolution of 300 m are obtained at approximately 10:00 GMT + 9 every one to two days. The OLCI has 21 spectral bands with wavelengths ranging from 400 to 1020 nm. OLCI level-1 data were downloaded from Copernicus Open Access Hub (<https://schub.copernicus.eu>). In this study, we used the Oa* reflectance (R_{rs}), CHL concentration, and total suspended matter (TSM) concentration of OLCI Level-2 water products. The Level-2 product was coordinate-transformed using the Case 2 Regional CoastColour (C2RCC) processor in the Sentinel Application Platform (SNAP, version 6.0) developed by the ESA. The C2RCC processor relies on a large database of radiative transfer simulations inverted by neural networks as its underlying technology (Brockmann et al., 2016).

2.3. Red tide information

Table 1 presents a list of outbreak information for HAB and non-HABs matched with OLCI images. This bloom occurred along the southern coast of Korea. For the ground-truth data, we used the red tide report provided by the NIFS (<https://www.nifs.go.kr/redtideInfo>) and relevant information. In the case of *M. polykrikoides* bloom as HAB, the red tide report by NIFS intensively provides approximate extents and locations during bloom outbreaks. However, information on non-HABs is often not provided by the NIFS. Therefore, we used the extent and cell abundance information obtained from relevant results on April 18 and 19, 2017 (Kim et al., 2020). We obtained 11 valid images matching the outbreaks of *M. polykrikoides* blooms and 10 valid images for non-HABs blooms. Eight HAB and 8 non-HABs images were used for training and testing, respectively, and three HAB images and two non-HABs images were used for validation. Non-HABs included *Alexandrium* sp., *Chattonella* sp., *Skeletonema* sp., *A. sanguinea*, *C. fruca*, and *M. rubrum* blooms. For validation, *Alexandrium* sp. and *M. rubrum* blooms were selected. The HAB and non-HABs maps as the ground-truth corresponding to 21 OLCI images were generated from HAB and non-HABs information of daily red tide report. Because this information is provided in polygon format, we converted into ground-truth maps in raster format. Each pixel is designated as a binary value indicating the nonexistence and existence of a red tide bloom.

Table 1

Outbreak information of HAB and non-HABs matched with OLCI images corresponding to ground-truth red tide map provided by National Institute of Fisheries Science (NIFS) and relevant information (Kim et al., 2020).

| | Red tide species | Acquisition dates | Data | Object |
|----------|--------------------------------------|---------------------|------------------------------|------------|
| HAB | <i>Margalefidinium polykrikoides</i> | July 29, 2018 | S3A_OL_1_EFR_20180729T015441 | Training |
| | | August 2, 2018 | S3A_OL_1_EFR_20180802T015057 | |
| | | August 3, 2018 | S3A_OL_1_EFR_20180803T012446 | |
| | | August 30, 2019 (A) | S3A_OL_1_EFR_20190830T020217 | |
| | | August 31, 2019 | S3A_OL_1_EFR_20190831T013606 | |
| | | September 17, 2019 | S3B_OL_1_EFR_20190917T015626 | |
| | | October 8, 2020 | S3A_OL_1_EFR_20201008T020225 | |
| | | October 13, 2020 | S3A_OL_1_EFR_20201013T013230 | |
| | | July 30, 2018 | S3A_OL_1_EFR_20180730T012830 | Validation |
| | | August 30, 2019 (B) | S3B_OL_1_EFR_20190830T012247 | |
| Non-HABs | <i>Alexandrium</i> sp. | October 17, 2020 | S3A_OL_1_EFR_20201017T012845 | |
| | | April 18, 2017 | S3A_OL_1_EFR_20170418T020210 | Training |
| | | August 12, 2017 | S3A_OL_1_EFR_20170812T015441 | |
| | | April 19, 2017 | S3A_OL_1_EFR_20170419T013559 | Validation |
| | | July 12, 2017 | S3A_OL_1_EFR_20170712T015825 | Training |
| | <i>Chattonella</i> sp. | October 10, 2019 | S3B_OL_1_EFR_20191010T020009 | Training |
| | | July 17, 2020 | S3A_OL_1_EFR_20200717T011349 | Training |
| | | May 19, 2021 | S3B_OL_1_EFR_20210519T014144 | Training |
| | | October 28, 2021 | S3B_OL_1_EFR_20211028T014146 | Training |
| | | November 3, 2021 | S3A_OL_1_EFR_20211103T012504 | |
| | <i>Mesodinium rubrum</i> | October 31, 2021 | S3B_OL_1_EFR_20211031T020413 | Validation |

2.4. Methods

To quantitatively discriminate of HAB and non-HABs, we first inspected visually using OLCI R_{rs} true-color composite images. Each image was compared to the ground-truth maps generated from the information of daily red tide report. We then investigated the spectra of HAB and HABs from OLCI according to the CHL concentration. A simple CNN model was trained and tested using training dataset of HAB and non-HABs generated from OLCI. Then, the performance of the generated CNN models was evaluated using validation dataset. Finally, we generated HAB and non-HABs map obtained from CNN model.

2.4.1. Dataset

In this study, CNN models were trained and tested to classify the OLCI patches into two labels, 1 and 0, as HAB and non-HABs, respectively. We used OLCI imagery with 16 spectral bands corresponding to the HAB and non-HABs maps as inputs. The output was labeled 1 for HAB and 0 for non-HABs. To generate patches, we used the point-marginal method. For HAB patches, each patch was created using the marginal pixels of the HAB pixels extracted from the corresponding ground-truth map. Non-HABs patches were generated using the surroundings of randomly selected pixels among non-HABs pixels. We obtained 10,987 HAB patches with sizes of $4 \times 4 \times 16$. To identify the effect of the non-HABs patches on the performance of the CNN model, four non-HABs datasets for training and testing were constructed, with HAB patches used in all models: (1) CNN-1 (32,961 non-HABs patches as three times HAB patches); (2) CNN-2 (54,935 non-HABs patches as five times HAB patches); (3) CNN-3 (76,909 non-HABs patches as seven times HAB patches); and (4) CNN-4 (98,883 non-HABs patches as nine times HAB patches). The patch number of CNN-1 was 43,948, including 10,987 HAB and 32,961 non-HABs patches, respectively. In the case of non-HABs patches, half were extracted from the images in which HAB occurred, and the other half was extracted from the images in which non-HABs occurred. For training and testing, patches for each CNN model were divided into 70 % and 30 %, respectively.

2.4.2. Convolution neural network

Fig. 2 shows the architecture of the CNN model used in this study. We used the developed CNN model developed by MathWorks (<https://www.mathworks.com/help/deeplearning/ug/create-simple-deep-learning-network-for-classification.html>). This example shows how to create and train a simple deep learning network for classification. Table 2 shows the CNN structure used in this study. For feature extraction, we first constructed with three convolution layers, three batch normalization layers, three rectified linear unit (ReLU) layers, and two max pooling layers. The basic formula of the convolution process is expressed by Eq. (1) (Tekerek and Yapici, 2022).

Table 2

CNN structures used in this study. The layers and options used in each order were described.

| Orders | Layers | Options |
|--------|---------------------------|--|
| 1 | Image Input Layer | Input size: $4 \times 4 \times 16$ |
| 2 | Convolution 2D Layer | Filter size: 3×3 Number of Filters: 8 Stride: 1×1 Mean Decay: 0.1 Variance Decay: 0.1 Epsilon: 0.00001 |
| 3 | Batch Normalization Layer | |
| 4 | ReLU Layer | Number of Inputs: 1 Number of Outputs: 1 |
| 5 | Max-Pooling 2D Layer | Pool size: 2×2 Stride: 2×2 |
| 6 | Convolution 2D Layer | Filter size: 3×3 Number of Filters: 16 Stride: 1×1 Mean Decay: 0.1 Variance Decay: 0.1 Epsilon: 0.00001 |
| 7 | Batch Normalization Layer | |
| 8 | ReLU Layer | Number of Inputs: 1 Number of Outputs: 1 |
| 9 | Max-Pooling 2D Layer | Pool size: 2×2 Stride: 2×2 |
| 10 | Convolution 2D Layer | Filter size: 3×3 Number of Filters: 32 Mean Decay: 0.1 Variance Decay: 0.1 Epsilon: 0.00001 |
| 11 | Batch Normalization Layer | |
| 12 | ReLU Layer | Number of Inputs: 1 Number of Outputs: 1 |
| 13 | Fully-Connected Layer | Output size: 2 |
| 14 | SoftMax Layer | Number of Inputs: 1 Number of Outputs: 1 |
| 15 | Classification Layer | Classes: 2 |

$$y_n = f \left(\sum_n x_n \times w_n + b_n \right) \quad (1)$$

In the equation, y , x , w , and b represent the pixels of the output image, the pixels of the input image, the pixels of the filter and the bias term, respectively. Then, ReLU as an activation function (f) is used after every convolution layer to model nonlinear operations. The ReLU function calculated by the formula given in Eq. (2).

$$\text{ReLU}(x) = \begin{cases} 0, & \text{if } x < 0 \\ x, & \text{if } x \geq 0 \end{cases} \quad (2)$$

The data in the previous layer can be represented by sub-samples through the pooling layer. Among the two frequently used pooling layer types, we used maximum pooling which produces a new pixel

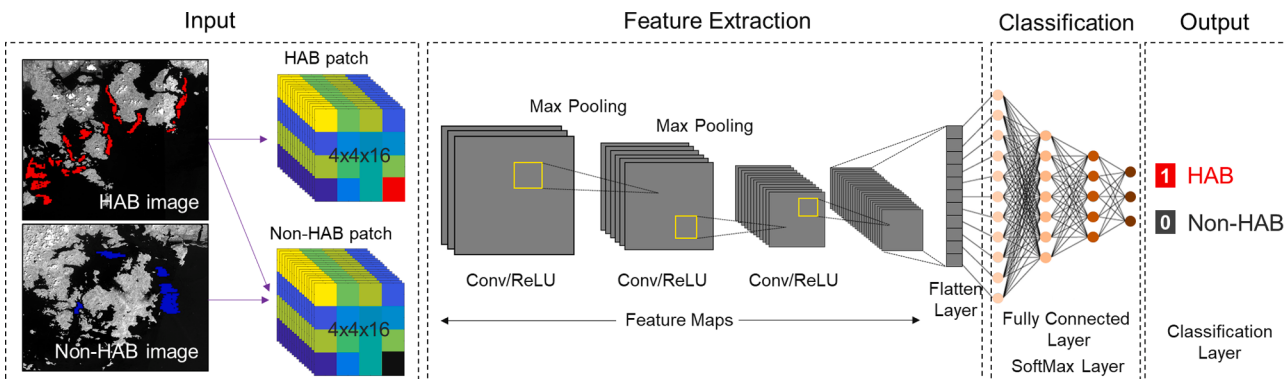


Fig. 2. Convolutional neural network (CNN) architecture for discriminating HAB and non-HABs. Training and test dataset were composed of Sentinel-3 OLCI R_{rs} images with 16 wavelength spectral bands as input. Input images were split OLCI R_{rs} images into $4 \times 4 \times 16$ sub regions. Output was labeled 1 and 0 for HAB and non-HABs, respectively. The network consists of input, feature extraction, classification, and output parts.

value by taking maximum values of the matching pixels in the input image.

For classification, fully-Connected layer and SoftMax layer were added. Fully-Connected layers formed by connecting the output neurons of the previous layers to each neuron in the next layer. Then, the results obtained from this layer are normalized to a probability distribution for the classification process using a SoftMax layer. Finally, the output was assigned to the classification layer. Training options were specified after defining the network structure. A stochastic gradient descent with momentum optimizer (Murphy, 2012) and an initial learning rate of 0.01 were used. The maximum number of epochs was 25. An epoch is the full training cycle for the entire training dataset. The shuffle option was applied at each epoch. The software calculated the accuracy of the validation data at regular intervals during training. The network was trained using a GPU with a fast processing speed.

2.4.3. Performance assessment

We qualitatively and quantitatively evaluated the performance of the CNN models. A qualitative assessment was performed using visual confirmation with the ground-truth maps provided by the NIFS. The CNN models were quantitatively validated by dividing the HAB and non-HABs datasets. For HAB, the five trained models were validated using 3,139 HAB and 3,139 non-HABs patches. These patches were extracted from OLCI images for the validation dataset (Table 1). We used a confusion matrix (Kohavi, 1998). The *rt* and *nrt* symbols in Table 3 indicate HAB and non-HABs from the ground truth, respectively, whereas *RT* and *nRT* indicate HAB and non-HABs in the predicted maps, respectively. Four figure-of-merits values (FOMs), sensitivity, precision, F-measure, and total accuracy were used. Sensitivity ($(4)/[(2)+(4)]$) and precision ($(4)/[(3)+(4)]$) were evaluated using only HAB from the ground truth and the predicted maps. The F-measure was calculated as $(2 \times \text{Precision} \times \text{Sensitivity}) / (\text{Precision} + \text{Sensitivity})$, which is called the harmonic mean. The total accuracy was expressed as $[(1)+(4)] / [(1)+(2)+(3)+(4)]$. On the other hand, when validating the CNN models using non-HABs images, these FOMs could not be used because there was no truth value in image. Thus, we calculated the error pixels of the predicted map when the model was applied to non-HABs image.

3. Results

3.1. Visual inspection of HAB and non-HABs

Fig. 3 shows various red tide bloom maps provided by the red tide report of the NIFS and the corresponding OLCI R_{rs} true-color composite images. In general, red tide patches caused by *M. polykrikoides* bloom appear reddish or brown in R_{rs} true-color composite images. Fig. 3a and b show the ground-truth distribution of the *M. polykrikoides* bloom and OLCI images collected on July 29, 2018 at 01:54 GMT along the coast of Goheung, Yeosu, and Namhae. According to the daily red tide report, red tide patches appeared sporadically along the coast between Goheung and Yeosu. In addition, a high-density red tide patch with 2,500 cells mL^{-1} was observed off the coast below Goheung. These patches were expressed more highly in the OLCI image than in the distribution of the

ground-truth map. Red tide bloom caused by *Alexandrium sp.* occurred on August 12, 2017 at 01:54 GMT off the coast of Tongyeong. According to daily red tide report, red tide density was up to 5,000 cells mL^{-1} . Although the red tide area was displayed in some areas on the ground-truth map, the OLCI image showed brown red tide patches spreading throughout the Tongyeong coast. Similarly, the OLCI image acquired on July 12, 2017, at 01: 58 GMT confirmed that the bloom caused by *Chattonella sp.* was brown and spread as a whole (Fig. 3e and f). The maximum density was 350 cells mL^{-1} . Red tide bloom caused by the diatom *Skeletonema sp.* is reddish (Matsuoka and Fukuyo, 2003). On October 10, 2019, it was reported that bloom occurred at a maximum cell density of 2,000 cells mL^{-1} in the form of dots or lines along the coast of Namhae (Fig. 3g). Red or brown blooms was confirmed in the OLCI image obtained on October 10, 2019 at 02:00 GMT (Fig. 3h). All four blooms changed the color of seawater to brown, and the remaining three blooms used in the study were the same.

3.2. Spectra of HAB and non-HABs from OLCI images

Fig. 4 shows the spectra of HAB and non-HABs from the OLCI images. We extracted the red tide spectral information from the OLCI-derived R_{rs} images (Table 1). We divided the spectral data into the following three CHL ranges of the subgroups based on the OLCI-derived CHL concentrations of 5 and 10 mg m^{-3} : high ($>10 \text{ mg m}^{-3}$), moderate ($5 \text{ mg m}^{-3} < \text{CHL concentration} < 10 \text{ mg m}^{-3}$), and low ($<5 \text{ mg m}^{-3}$). In general, when red tide blooms did not occur, the CHL concentration did not exceed 5 mg m^{-3} (Shin et al., 2019), so the standard of the low CHL subgroup was set to 5 mg m^{-3} . In addition, considering the CHL concentration value with high cell density, the high CHL subgroup was set to 10 mg m^{-3} . The extracted spectrum for each range was averaged for each red-tide bloom. All spectra showed the peak value at 560 nm, which it tended to decrease towards shorter wavelengths. Each subgroup for each red tide bloom showed similar spectral patterns. The spectrum intensity was usually the largest for low subgroups and the smallest for high subgroups. This is because absorption at short wavelengths increases with increasing CHL concentration increases (Dierssen et al., 2006; Ryan et al., 2009). Other red tide species, except *Alexandrium sp.*, had high CHL subgroups. Unlike the two subgroups, some spectra of the high subgroups showed a peak at 709 nm. This was particularly evident in the case of *Skeletonema sp.* (Fig. 4e) and *C. furca* (Fig. 4g) blooms. This peak was due to the fluorescence properties of phytoplankton. Overall, as shown in Fig. 3h and i, the spectra in the low and moderate subgroups showed a similar pattern, but those between 510 and 620 nm were slightly different. This suggests that the spectrum of red tide bloom is first determined by the type of bloom, but if the optical properties between the type of bloom are similar, the spectral shape with a particular peak or intensity is determined by CHL concentration, the magnitude of bloom, or other factors.

3.3. CNN models for discriminating HAB and non-HABs

Table 4 shows the performance of the four CNN models for HAB. The CNN-1 model trained with the fewest non-HABs patches showed the highest sensitivity (0.69), whereas the CNN-4 model, trained with the most patches, showed the highest precision level (0.92). This means that the higher the number of non-HABs patches for training, the less overestimated the predicted red tide area. The sensitivity and precision of the two FOMs were complementary to each other, and the F-measure level (0.75) and total accuracy (0.77) was the highest in the CNN-1 model. The CNN-4 model had the F-measure and total accuracy with the second highest value. In terms of false positives (336), the CNN-4 model showed the best performance.

Fig. 5 shows the ground-truth HAB maps and the predicted HAB maps generated from the CNN-1 and CNN-4 models. In the case of the predicted HAB maps generated from the CNN-1 model, the areas were overestimated compared to the ground-truth HAB maps. As shown in

Table 3
Confusion matrix for evaluating CNN models.

| | | Ground truth | | <i>Precision</i> $(4)/[(3)+(4)]$ | <i>Sensitivity</i> $(4)/[(2)+(4)]$ |
|-------------------|----------------------|----------------------|--------------------|-------------------------------------|---------------------------------------|
| | | False (<i>nrt</i>) | Ture (<i>rt</i>) | | |
| Predicted results | False (<i>nRT</i>) | (1) True negative | (2) False negative | | |
| | True (<i>RT</i>) | (3) False positive | (4) True positive | | |
| | | | | | |

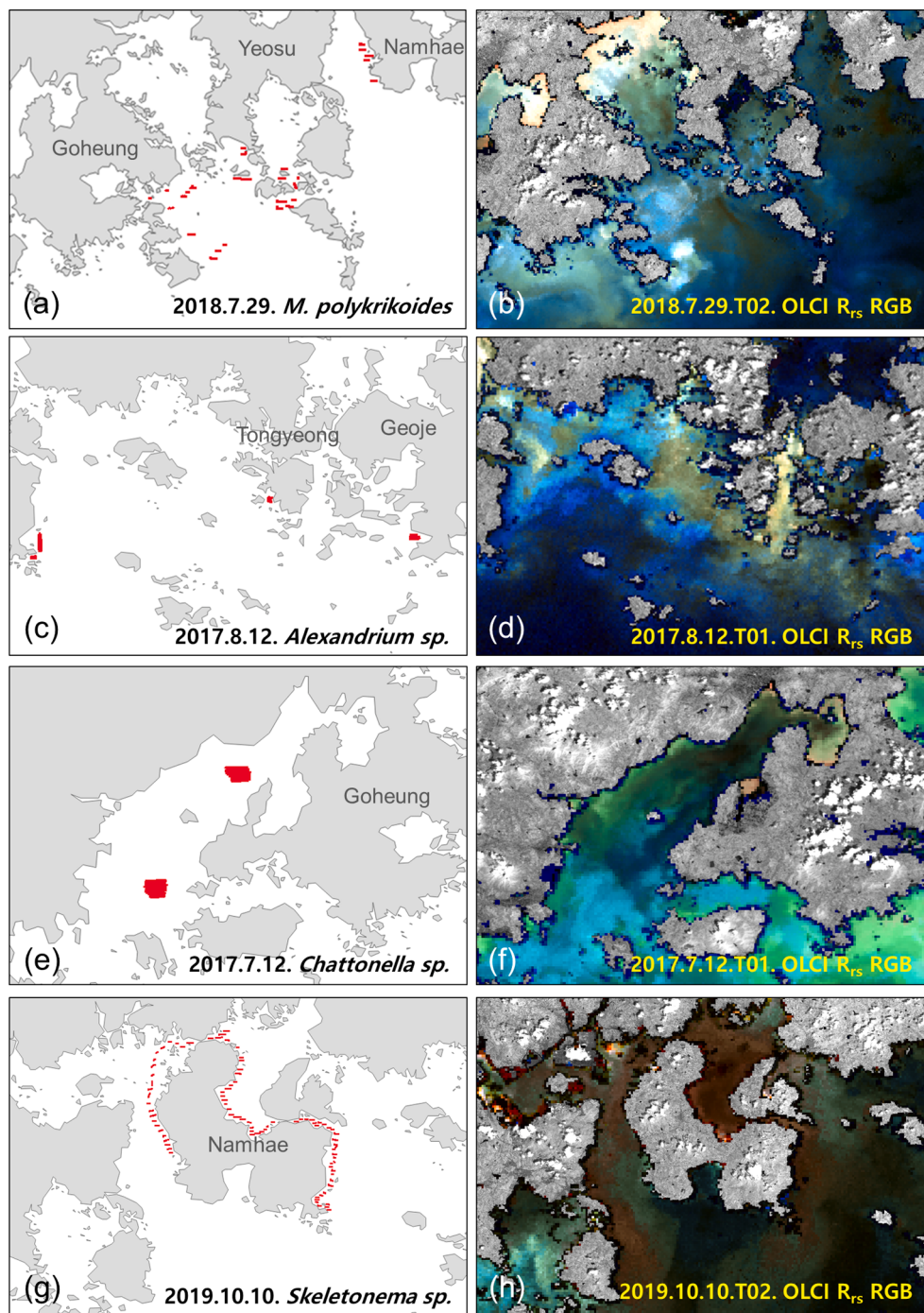


Fig. 3. Various red tide bloom maps provided by NIFS and OLCI remote sensing reflectance (R_{rs}) true-color composite image (R: 681.25; G: 560; B: 442.5 nm). (a) and (b) represent *M. polykrikoides* bloom as HAB. (c)–(h) shows non-HABs including *Alexandrium sp.*, *Chattonella sp.*, and *Skeletonema sp.*. Likewise, the date of collection is indicated on the image. (For interpretation of the references to color in this figure legend, the reader is referred to the web version of this article.)

Table 4, these results can be described as having a high sensitivity level in CNN-1 model. However, the predicted HAB maps showed a distribution similar to that of the red tide patches in each ground-truth map. The ground-truth map is generally displayed in a lumped form, whereas the predicted map simulates a more detailed distribution with a spatial resolution of 300 m.

Fig. 6 shows the validation results of CNN-1 and 4 models using non-HABs images. **Fig. 6a** and d show the ground-truth maps of *M. rubrum* and *Alexandrium sp.* blooms which occurred along the coast of Yeosu and Geoje, respectively. When non-HAB caused by *M. rubrum* occurred, we calculated the number of error pixel. In the case of the images in which

M. rubrum blooms occurred, the number of error pixels was similar (CNN-1 model: 45.54 km²; CNN-4 model: 44.19 km²). In addition, patterns of pixels recognized as HAB were distributed similarly to patches of *M. rubrum* bloom. On the other hand, in the case of *Alexandrium* bloom, the predicted HAB map estimated from CNN-4 model (1.71 km²) had fewer HAB pixels compared to CNN-1 model (33.39 km²) (**Fig. 6e** and f). These results were the same as those obtained by applying the model to the HAB image. This suggests that more non-HABs patches can be used to reduce errors in the trained model. Considering these results comprehensively, we chose the CNN-4 model as the most reasonable model for discriminating HAB and non-HABs.

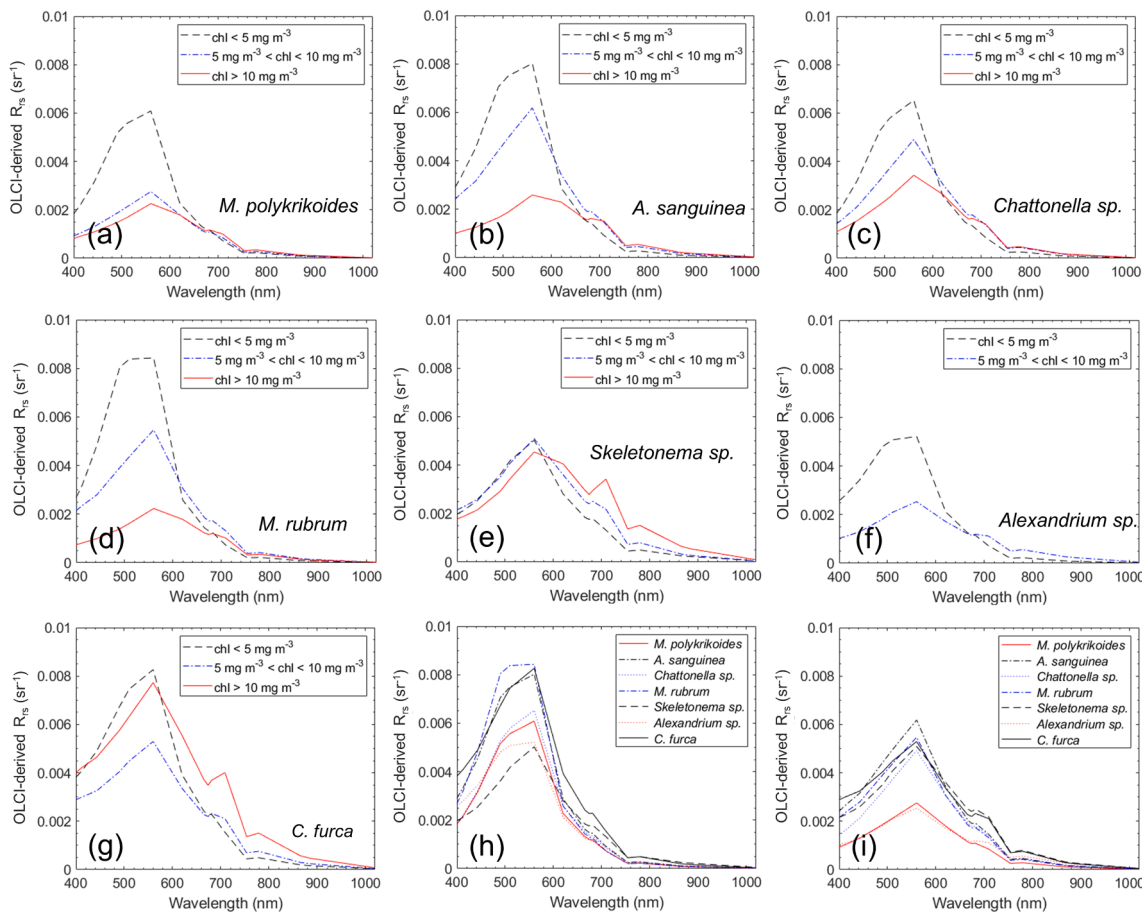


Fig. 4. Spectra of HAB and non-HABs from OLCI-derived remote sensing reflectance (R_{rs} , sr^{-1}). HAB means (a) *M. polykrikoides* bloom. Non-HABs are caused by (b) *A. sanguinea*, (c) *Chattonella* sp., (d) *M. rubrum*, (e) *Skeletonema* sp., (f) *Alexandrium* sp., and (g) *C. furca*. The spectra were divided into three subgroups according to a range of OLCI-derived chlorophyll (CHL) concentration. The black dashed lines, blue dash-dotted lines, and red solid lines represent the low ($<5\text{ mg m}^{-3}$), moderate ($5\text{ mg m}^{-3} < \text{CHL concentration} < 10\text{ mg m}^{-3}$), and high ($>10\text{ mg m}^{-3}$) subgroups, respectively. The spectrum for each subgroup were averaged. (h) and (i) show low and moderate subgroups for each bloom, respectively. (For interpretation of the references to color in this figure legend, the reader is referred to the web version of this article.)

Table 4
Performance evaluation of five CNN models using the validation dataset for HAB.

| Models | Training pixel numbers | | (1) | (2) | (3) | (4) | Sens. | Prec. | FM | Accu. |
|--------|------------------------|----------|-------|-------|-----|-------|-------|-------|------|-------|
| | HAB | Non-HABs | | | | | | | | |
| CNN-1 | 10,987 | 32,961 | 2,667 | 967 | 472 | 2,172 | 0.69 | 0.82 | 0.75 | 0.77 |
| CNN-2 | 10,987 | 54,935 | 2,954 | 1,588 | 185 | 1,551 | 0.49 | 0.89 | 0.64 | 0.72 |
| CNN-3 | 10,987 | 76,909 | 2,938 | 1,613 | 201 | 1,526 | 0.49 | 0.88 | 0.63 | 0.71 |
| CNN-4 | 10,987 | 98,883 | 2,993 | 1,482 | 146 | 1,657 | 0.53 | 0.92 | 0.67 | 0.74 |

* (1): true negative; (2): false negative; (3): false positive; (4): true positive; Sens.: sensitivity; Prec.: precision; FM: F-measure; Accu.: total accuracy.

4. Discussion

4.1. Occurrence tendency of red tide blooms

The species causing red tides on the Korean coasts have changed considerably over the past four decades (Lee et al., 2013). In the 1970s, diatoms, *Skeletonema* sp. and *Chaetoceros* spp. were the three most dominant red tide taxa, accounting for 73 % of all red tide events in Jinhae Bay. However, the transition from diatoms to dinoflagellates occurred in the 1980s. The first record of fish killed by red tide in Korea was caused by *Karenia mikimotoi*. In 1982, red tide blooms in Jinhae Bay were caused by the ichthyotoxic mixotrophic dinoflagellate *M. polykrikoides*, previously known as *Cochlodinium polykrikoides* (Gómez et al., 2017). In the 1990s, the dinoflagellate species causing red

tides shifted from those that killed fish to those that did not. In 1993, large-scale blooms caused by *M. polykrikoides* began to appear. Massive *M. polykrikoides* blooms (maximum cell density, 30,000 cells mL^{-1}) occurred in 1995, affecting many near-shore areas on the southern coast of the Korean Peninsula. Over the past decadal, incidence of *Skeletonema* sp., *Chaetoceros* spp., and *K. mikimotoi* blooms has generally decreased, whereas that of *M. polykrikoides*, *Alexandrium* sp., *Ceratium* spp., and *N. scintillans* blooms has increased. In the 2000s, *M. polykrikoides* remained the dominant red tide species and *N. scintillans*, *Heterosigma akashiwo*, and *Prorocentrum dentatum* blooms also occurred around the Korean Peninsula (NIFS, 2015). The suitable conditions for red tide species to cause blooms differ. HAB caused by *M. polykrikoides* frequently occurs off the southern coast of Korea and are mostly initiated when the water temperature reaches approximately 25 °C during the

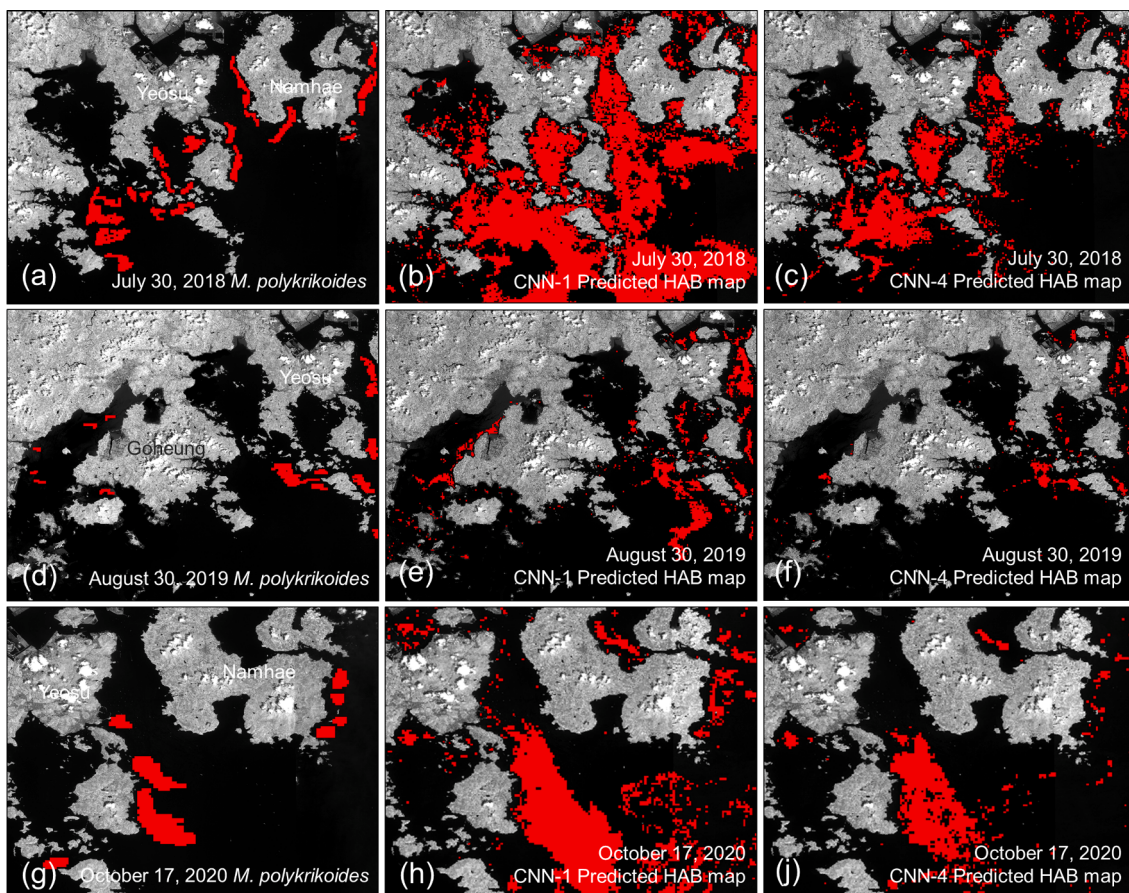


Fig. 5. Validation results estimated from CNN-1 and 4 models using HAB images. (a), (d), and (g) represent the ground-truth maps of *M. polykrikoides* bloom at each date provided by NIFS. (b)-(j) represent the predicted map generated from CNN-1 and 4 models. The acquisition date of map is indicated for each image.

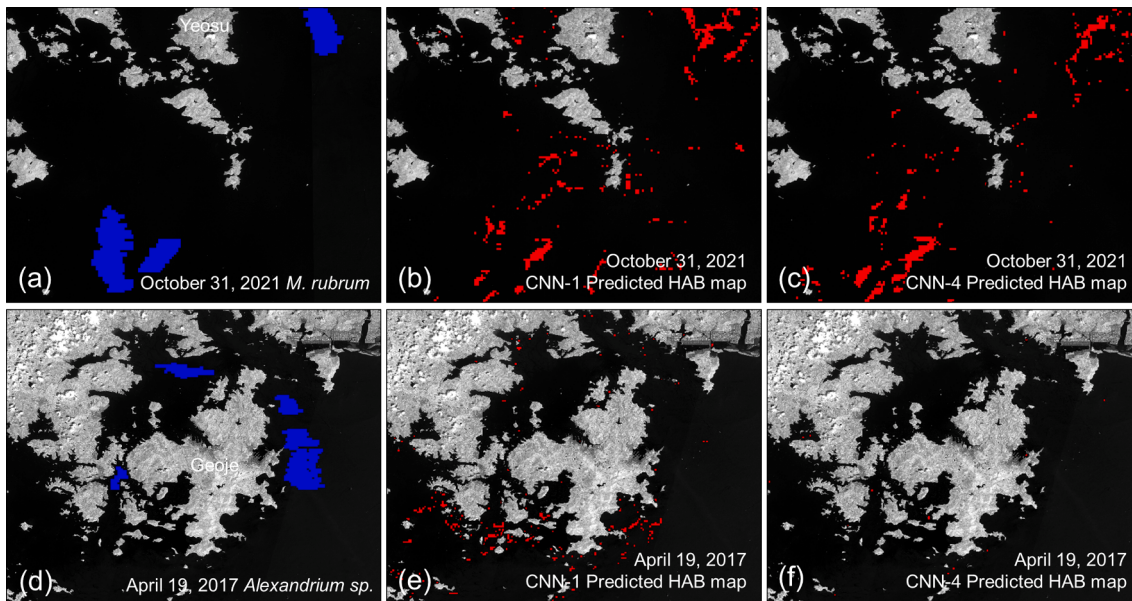


Fig. 6. Validation results estimated from CNN-5 model using non-HABs images. (a) and (c) represents non-HABs ground-truth maps of *M. rubrum* (on October 31, 2021) and *Alexandrium sp.* (on April 19, 2017). (b) and (d) are the predicted HAB maps generated from CNN-5 model. Blue and red pixels indicate non-HABs and HAB pixels, respectively. (For interpretation of the references to color in this figure legend, the reader is referred to the web version of this article.)

summer season (Shin et al., 2019). However, *M. polykrikoides* bloom can sometimes start at the end of September and last until October. The diatom *Skeletonema sp.* breeds in coastal and brackish waters and causes

red tide bloom every year on all coasts of Korea. It forms a large cell during winter and spring but miniaturizes at high temperatures (Mat-suoka and Fukuyo, 2003). Off the coast of Korea, *Skeletonema sp.* bloom

frequently occur in the spring, autumn, and winter. Dinoflagellate and diatoms engage in interspecific competition. If a suitable environment for the growth of dinoflagellates is created due to the reduction of diatoms and proper water temperature, the density of dinoflagellates can increase. In contrast, following long rainfall, diatoms become the dominant species (NIFS, 2015). Even in the absence of interspecific competition, the non-HABs studied here occur in the same waters as HAB. Red tide blooms overlapped temporally and mixed spatially. Blooms of *Chattonella sp.* and *M. polykrikoides* occurred simultaneously off the coast near Goheung (Fig. 1) on July 24 and 25, 2018. The difference between these two blooms, and thus discrimination between HAB and non-HABs, could not be determined by visual inspection and spectrum analysis. To avoid these complex problems, we only selected cases where only one red tide bloom occurred predominantly on that date.

4.2. Recognition limit of red tide blooms

The recognition limit refers to the level at which a red tide bloom can be identified visually. The density of red tide species that can change seawater color depends on the size, cell volume, and content of CHL in the cell. The recognition limit of red tide blooms by density is approximately 10^4 microplankton and 10^5 nanoplankton in 1 mL of seawater (Park et al., 1985). *Skeletonema sp.* is a micro-diatom but causes seawater color change with a density of 10^5 cells mL^{-1} because of the wide difference in cell size. *N. scintillans*, a macro dinoflagellate, changes seawater color at a density below 1,000 cells mL^{-1} . The cell volume due to the initial density when red tides are formed varies depending on red tide species and density (Kim et al., 1993). *H. akashiwo*, a micro-dinoflagellate, had cell volumes of 1.3×10^6 and $115.8 \times 10^6 \mu\text{m}^3 \text{mL}^{-1}$ at red tide densities of 1,300 and 112,360 cells mL^{-1} , respectively. The cell volumes of *M. polykrikoides* were 5.3×10^6 and $50.1 \times 10^6 \mu\text{m}^3 \text{mL}^{-1}$ at 920 and 8,700 cells mL^{-1} , respectively. These results show that the cell volumes of the same red tide species can vary greatly depending on the density. In the case of phytoplankton, seawater color changes are related to the CHL pigment content of the red tide species. Ahn et al. (2009) estimated CHL quantities per unit cell for 21 red tide species. They reported that *M. polykrikoides* had the largest value of $1.6 \times 10^{-1} \mu\text{g cell}^{-1}$ and *Chattonella sp.* had the smallest value of $4.2 \times 10^{-2} \mu\text{g cell}^{-1}$. In Korea, the issuance standard of red tide warnings was set at a red tide recognition limit of 1,000 cells mL^{-1} . This is because the cell length of *M. polykrikoides* which frequently causes red tide blooms, is $>30 \mu\text{m}$ (Park et al., 1985). Standards are also in place for other red tide species, but in most cases, only *M. polykrikoides* warnings are issued. According to the recognition limit, to change seawater color, a higher density is required than a species with a larger cell size. In Fig. 2, the red tide blooms change the seawater color, allowing them to be discriminated from the surrounding waters. The density of *Skeletonema sp.*, a microplankton, was approximately 2,000 cells mL^{-1} , whereas that of *Chattonella sp.*, a macroplankton, was only 350 cells mL^{-1} . In both cases, we could visually confirm the changes in seawater color. This means that the larger the cell size, the lower the density required to change the seawater color.

4.3. CHL and TSM concentrations of red tide blooms

We found that the high subgroups of *Skeletonema sp.* and *C. furca* blooms showed a peak at 709 nm, which is due to the fluorescence properties of phytoplankton. These results are consistent with those of the previous studies. Shin et al. (2019) investigated the in-situ R_{rs} patterns of *M. polykrikoides* measured during a field survey. They found that the spectrum with an in situ CHL concentration over 10 mg m^{-3} had a sharper slope between the green and red wavelengths than those with CHL concentrations below 10 mg m^{-3} . Their spectra showed peaks near 570 and 710 nm. Gitelson (1992) found a shift in the peak position from

approximately 680 up to 715 nm and an increase in the peak magnitude when the CHL concentration was increased. The magnitude and peak position can be used as precise indicators and predictors of phytoplankton concentrations and these contributed significantly to increasing the accuracy of the derivation of CHL values from the multispectral data. Gower et al. (2005) and Noh et al. (2018) reported that the center wavelength of the red-edge like peak migrated toward 710 nm as the CHL concentration increased over 100 mg m^{-3} . In agreement with past studies, our results revealed changes in the multispectral bands according to the CHL concentration for each red tide bloom. To confirm the CHL concentration corresponding to red tide blooms, we investigated the OLCI-derived CHL concentrations of the pixels where HAB and non-HABs occurred. Fig. 7a shows histograms of the CHL concentration pixels extracted from the seven red tide blooms. A total of 100 pixels were randomly selected from the pixel groups for each red tide bloom. Except for *Skeletonema sp.*, the six groups showed similar ranges of CHL concentrations. Fig. 7b shows the maximum CHL concentration for each bloom. *Skeletonema sp.* and *Alexandrium sp.* blooms had the highest and lowest maximum CHL concentrations, at 73.37 mg m^{-3} and 5.66 mg m^{-3} , respectively, while *C. furca* bloom showed the second highest CHL concentration at 16.5 mg m^{-3} . As shown in Fig. 4, the spectra of *Skeletonema sp.* and *C. furca* blooms in the high subgroups showed distinct characteristics at 709 nm. This is because the two blooms occurred at a higher density than the other blooms and thus this feature cannot be recognized as an optical property of each red tide bloom.

In addition, we confirmed that the spectra for the low and moderate CHL subgroups showed a similar patterns at all wavelengths (Fig. 4h and i). However, there were differences in the peak intensity and spectral shape between 510 and 620 nm for each red tide species. This may be due to the differences in TSM in the waters where blooms occurred, rather than the optical properties of each red tide species. Fig. 8 shows the spectra of various red tide blooms from the OLCI-derived R_{rs} according to the range of TSM concentrations. For this purpose, the OLCI-derived TSM concentration for each red tide bloom pixel was used. In all red tide blooms (Fig. 8a-g), the higher the TSM concentration, the greater the slope between 510 and 560 nm. Wavelength bands between 510 and 620 nm have been used for estimating TSM (Baban, 1993; Eleveld et al., 2008; Miller and McKee, 2004). Fig. 8h and i show the mean spectra of the low and moderate subgroups, respectively. The spectra of the moderate subgroups were more similar than those of the low subgroups. CHL and TSM concentration levels caused by red tide blooms are determined by several factors, such as cell density, CHL content in cells, and the size of red tide species; therefore, the type of red tide species cannot be directly determined based on CHL and TSM concentration levels. The concentrations of CHL and TSM have a positive correlation, with an R^2 of 0.11–0.73. To solve the problem of determining the type of red tide bloom through CHL and TSM concentrations, CNN model is capable of defining an ambiguous relationship between the spectrum and the type of red tide bloom may be effective.

Differences between various red tide blooms cannot be detected by multi-spectrum sensors with low spectral resolution and few band numbers. Fluorescence band are not included in the MODIS and GOCE sensors. On the other side, the Envisat Medium Resolution Imaging Spectrometer (MERIS) sensor is designed for the use of the signal from CHL fluorescence stimulated by ambient sunlight to detect and map phytoplankton (Gower and King, 2007; Zhao et al., 2015). This is especially useful for coastal waters, which are complicated by the high concentrations of gelbstoff and TSM. The spectrum signal was determined by absorption by pure water, scattering by TSM, and absorption and fluorescence of CHL. Spectral channels centered at 665, 681, and 705 nm were included in MERIS for retrieving the fluorescence signal. OLCI is a continuation of MERIS and improves on MERIS as it has six additional spectral bands, a higher signal-to-noise ratio (SNR), reduced solar glaring, an improved maximum spatial resolution of 300 m, and increased ground coverage, allowing it to sense phytoplankton and other organisms in the ocean. Like MERIS, OLCI has four spectral channels,

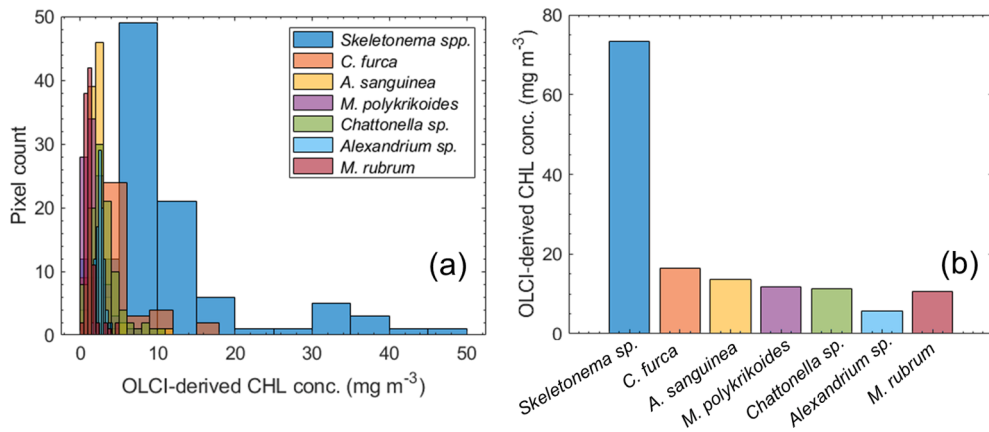


Fig. 7. (a) Histograms of OLCI-derived CHL concentrations from various red tide blooms. (b) Maximum CHL concentration of various red tide bloom. 100 pixels were selected randomly from pixel groups for each red tide bloom. (For interpretation of the references to color in this figure legend, the reader is referred to the web version of this article.)

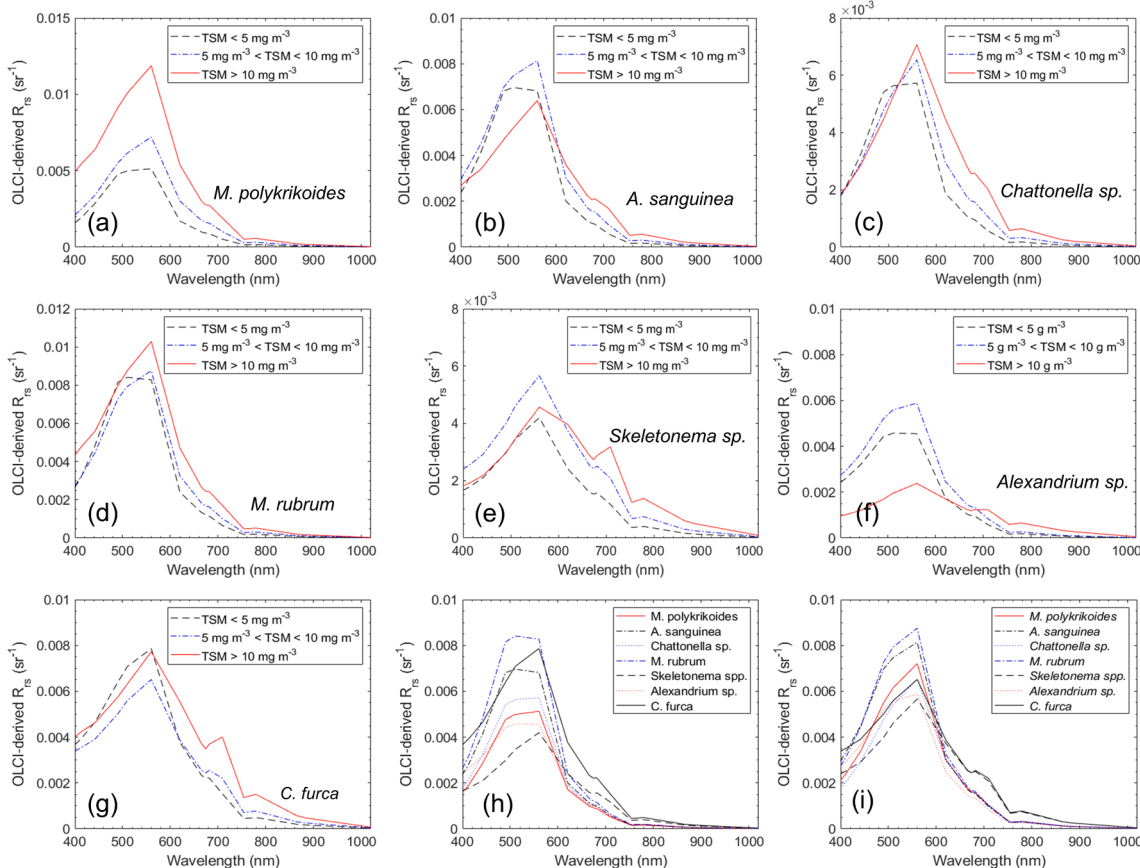


Fig. 8. Spectra of red tide blooms from OLCI-derived R_{rs} according to TSM concentration. (a)-(g) represents each red tide bloom. The spectra were divided into the three subgroups according to a range of OLCI-derived total suspended matter (TSM) concentration. The black dashed lines, blue dash-dotted lines, and red solid lines represent the low ($< 5 \text{ mg m}^{-3}$), moderate ($5 \text{ mg m}^{-3} < \text{TSM} < 10 \text{ mg m}^{-3}$), and high ($> 10 \text{ mg m}^{-3}$) subgroups, respectively. The spectrum for each subgroup were averaged. (h) and (i) represent the spectra of low and moderate subgroups, respectively. (For interpretation of the references to color in this figure legend, the reader is referred to the web version of this article.)

centered at 665, 674, 681, and 709 nm, for retrieving the fluorescence signal. In addition, OLCI has a subdivided wavelength band at approximately 560 nm with a high spectral resolution. As shown in Figs. 4 and 8, the mean spectra for each CHL and TSM subgroup showed a similar pattern, but the peaks near 560 and 709 nm differed slightly. The information provided by these wavelength bands can help train the CNN model.

4.4. Ambiguity of red tide index

To confirm the performance of the CNN model, we applied three red tide indexes to the validation images. First, using wavelength bands of 490 and 560 nm based on OLCI, the feasibility of red tide detection (FRTD) index proposed by Suh et al. (2004) detected increase in suspended particulate matter caused by *M. polykrikoides*

bloom. The equation used was $-11.51 \times \ln(nL_w(490)/nL_w(560)) + 14.38$. An FRTD index value above 15 indicates a red tide bloom. Second, the spectral shape (SS) index developed by Tomlinson et al. (2009) uses 443, 490, and 510 nm-based OLCI. The equation used was $nL_w(490) - nL_w(443) - [(nL_w(510) - nL_w(490)) \times (490 - 443)/(510 - 443)]$. This index has been used to detect *M. polykrikoides* and *Karenia brevis* (Shin et al., 2017; Shin et al., 2019; Son et al., 2012; Tomlinson et al., 2004). A negative SS index value indicates a red tide bloom. The maximum CHL index (MCI) utilizes the fluorescence properties of phytoplankton near 709 nm (Gower et al., 2005). This index uses 681, 709, and 754 nm-based OLCI. The equation used was $L_w(709) - L_w(681) - [(709 - 681) \times (L_w(754) - L_w(681))/(754 - 681)]$. It shifts to longer wavelengths with increasing bloom intensity (Dierssen et al., 2006; Schalles, 2006). MCI values tend to be negative where peaks occur near 685 nm but positive where the peak has shifted to longer wavelengths, up to approximately 705 nm. With reference to this, we used positive values for a red tide bloom. While the FRTD and SS indexes use the blue and green wavelength bands, MCI uses the fluorescence bands.

Fig. 9 shows the validation results estimated from the FRTD, SS, and MCI. Compared to the ground-truth of the *M. polykrikoides* bloom shown in Fig. 5a, the estimated HAB distribution was overestimated for all indexes. Most of the areas surrounding the coast were recognized as HAB. The F-measure levels were in the range of 0.02–0.05. In fact, when these index values based on band combination were used for training of CNN model as input, we found that the performance was lowered or the training was not good. Therefore, we only used the OLCI 16 bands as input. In non-HABs images, the map calculated from the FRTD showed the greatest error pixel number compared to the predicted map shown in Fig. 6b and d (*M. rubrum*: 5,400; *Alexandrium sp.*: 25,720). The SS and MCI had low error pixel numbers and some pixels estimated from the indexes were non-HABs pixels (Fig. 6a and c). The red tide index detected both HAB and non-HABs pixels and the coastal area was recognized as a red tide bloom. These results indicate that the wavelength bands used in the red tide index responds to red tides and TSM or other seawater components. Adjusting the threshold of the index to

reduce overestimation is not easy to apply to actual images because it varies greatly from image to image. Compared with these results, our CNN model had the advantage that the coastal region was not recognized as a red tide and did not require a fluid threshold. Fig. 10 shows the scatter plot of conventional red tide indexes, including FRTD, SS, and MCI. The distribution of *M. polykrikoides* bloom overlapped significantly with those of other red tide bloom and the discrimination of red tide blooms through these indexes was ambiguous. Because distributions can vary according to the intensity of occurrence for each red tide bloom, it is difficult to use distribution as an indicator for the discrimination of red tide blooms.

4.5. Performance of CNN model

In fact, the tendency between the F-measure and the total accuracy is irrelevant. This is because the two FOM are calculated differently. The total accuracy refers to the ratio of the sum of true negative and true positive among the total number of samples. The F-measure is the harmonic mean that is calculated from Sensitivity and Precision. When true negative increases, the total accuracy increases, but the F-measure does not increase. In the case of red tide detection, it is reasonable to consider the F-measure value rather than the total accuracy because red tide region is generally overwhelmingly less than non-red tide region in the image. Shin et al. (2021) mentioned that the tendency of the F-measure and the total accuracy did not coincide when they calculated the FOMs for *M. polykrikoides* detection. In addition, when red tide blooms were detected with images with spatial resolution of 300–500 m, such as GOCI and OLCI, the F-measure value was calculated about 0.3 unlike images with high spatial resolution of 1–10 m (Shin et al., 2019). Therefore, we selected the model based on the F-measure level and the predicted map. The CNN-4 model, which we finally chose, showed the performance with the FOMs of 0.53 for sensitivity, 0.92 for precision, and 0.67 for F-measure. This is higher than the F-measure level of *M. polykrikoides* detection with the same level of spatial resolution (Shin et al., 2019).

Several factors can affect the performance of CNN models. First, the

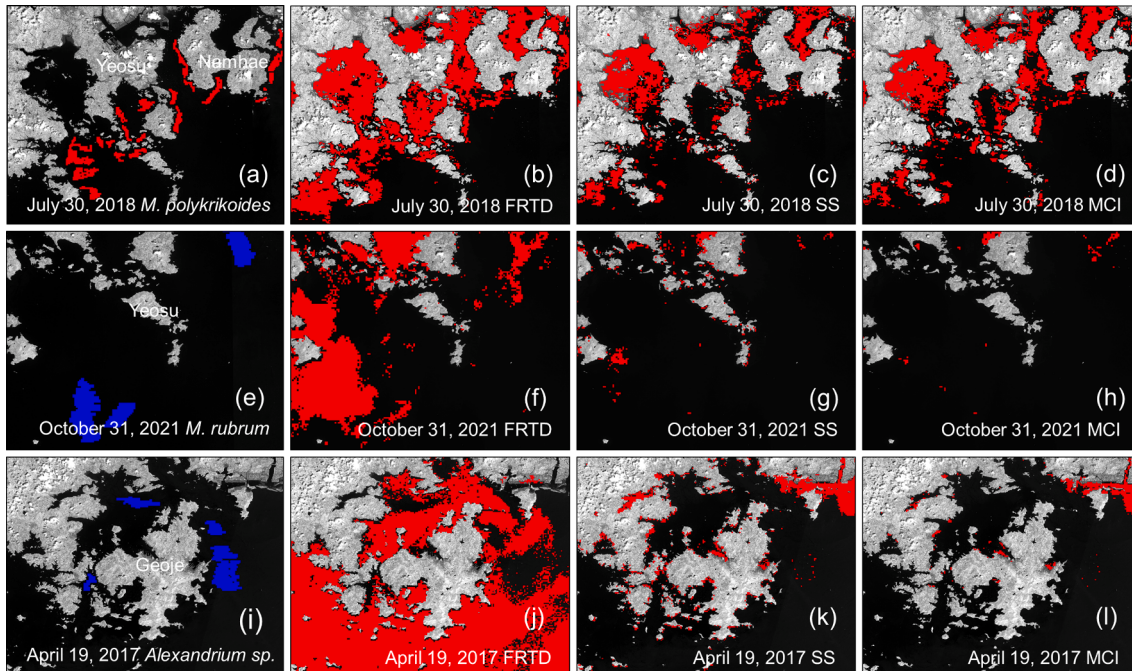


Fig. 9. Validation results estimated from three red tide indexes: FRTD, SS, and MCI. (a), (e), and (i) represent the ground truth maps of HAB and non-HABs. (b)–(d) showed HAB distribution generated using HAB image obtained on July 30, 2018. (f)–(h) and (j)–(l) are HAB maps generated using non-HABs images of *M. rubrum* (October 31, 2021) and *Alexandrium sp.* (April 19, 2017) blooms. (For interpretation of the references to color in this figure legend, the reader is referred to the web version of this article.)

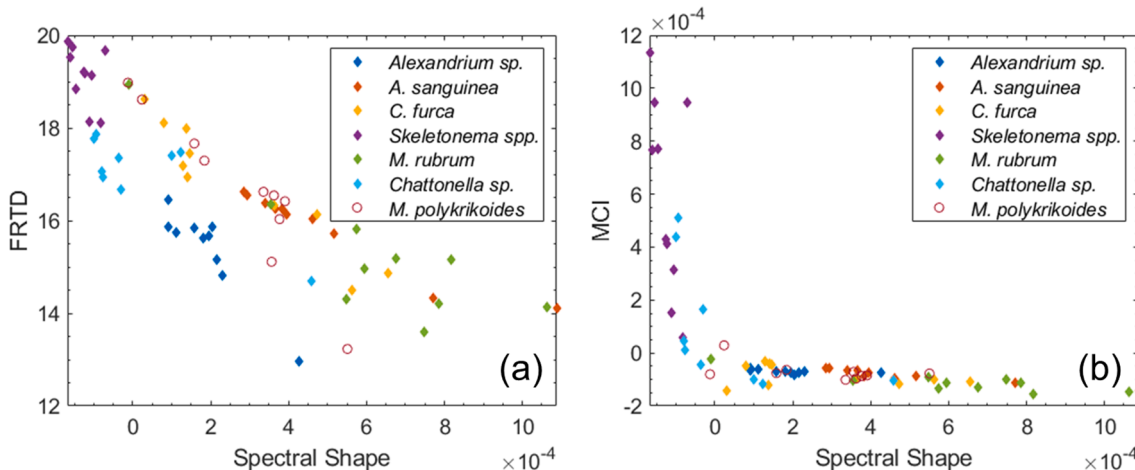


Fig. 10. Scatter plots between conventional red tide indexes. (a) Spatial distribution between spectral shape (SS) and feasibility of red tide detection (FRTD) indexes for seven red tide blooms. (b) Relationship between SS and MCI. Red circles are *M. polykrikoides* bloom. Diamonds are other blooms. (For interpretation of the references to color in this figure legend, the reader is referred to the web version of this article.)

difference in acquisition time between the ground-truth map and OLCI image may affect performance. The daily red tide reports provided by the NIFS are created from field surveys and fishermen's reports. Therefore, the data on extent of distribution throughout the day are approximate. However, OLCI images were acquired between approximately 10:00 and 11:00 GMT + 9. As shown in Fig. 4, owing to this difference, the red tide area of the ground-truth map may not be recognized as a red tide in the CNN model. Second, the intensity of red tide blooms may affect CNN model performance. In this study, we trained a CNN model using red tide blooms above the recognition limit. However, because the spatial distribution of the ground-truth also includes a red tide patch below the recognition limit, this may not be considered in our model. Third, the occurrence of mixed red tides can lower the performance of the model. For training, we used only cases of single red tide bloom. However, mixtures of two or three red tide blooms are common and are not included in the daily reports. Therefore, when red tide blooms are mixed, the performance of the CNN model may decrease. Fourth, a limited number of non-HABs can affect model performance. Non-HABs, or blooms other than *M. polykrikoides* bloom are usually not reported in detail in daily red tide reports. Therefore, we used only a limited number of images for training. Validation was possible only in two cases of *M. rubrum* and *Alexandrium sp.* blooms, in which image acquisition for several days was possible. In fact, the ratio of the patch number between HAB and non-HABs affected the performance of the CNN model. We found that the performance improved quantitatively and qualitatively as the number of non-HABs patches increased. To identify the effectiveness of the non-HABs patches, we trained and evaluated a model (CNN-5) consisting of 10,987 HAB patches and 98,883 non-HABs patches that did not include patches extracted from other red tide blooms except *M. polykrikoides* bloom. Non-HABs patches consisted only of patches from the images of *M. polykrikoides* bloom. The CNN-5 model exhibited the lowest F-measure (0.31). In particular, when this model was applied to non-HABs images, areas of non-HABs were incorrectly recognized as HAB, indicating that there was little distinction between bloom types. Additionally, when we increased the number of non-HABs patches in the CNN-4 model, there was no significant improvement over the previous models. Therefore, we finally selected the CNN-4 model considering the training time.

5. Conclusions

In this study, a CNN model was proposed to discriminate *M. polykrikoides* HAB from various red tide blooms as non-HABs off the southern coast of Korea using OLCI images. The main results were as

follows: (i) visual inspection of OLCI images revealed that red tide patches caused by red tide blooms appeared reddish or brown in the R_{rs} true-color composite images. The spectra of HAB and non-HABs showed similar patterns according to the CHL concentration. (ii) Among the five CNN models with different non-HABs patches, the CNN-4 model trained with the most non-HABs patches showed the most reasonable performance quantitatively and qualitatively. Our results showed that the CNN model can reduce false alarms in coastal areas from a similar spectral response due to turbid waters, without restrictions on the threshold value of the red tide index.

Until now, ocean color sensors, such as MODIS, VIIRS, and GOFCI, have mainly been used for HAB monitoring; however, these sensors have limited spatial resolution and accessibility. In particular, the waters off the southern coast of Korea have many islands and complex coastlines. Our results showed that OLCI images with a spatial resolution of 300 m were effectively for monitoring red tide blooms off the Korean coast. Following Sentinel-3A and 3B, Sentinel-3C and 3D are scheduled to be launched in 2023 and 2025, respectively, to ensure the continuity of the Sentinel-3 mission. Our study used images from Sentinel-3A and 3B. In the future, Sentinel-3C and 3D images can be incorporated for improved HAB monitoring. In conclusion, the proposed CNN model using OLCI images can contribute to an effective disaster prevention system to minimize the damage caused by HABs. In addition, this model can be a basis for research on the discrimination of red tide blooms using aircraft-based hyperspectral images with considerable spectral information.

Declaration of Competing Interest

The authors declare that they have no known competing financial interests or personal relationships that could have appeared to influence the work reported in this paper.

Acknowledgements

This study was supported by the project titled "Development of technology using analysis of ocean satellite images" (20210046) and "UAV-based marine Safety, Illegal Fishing and Marine Ecosystem Management Technology Development" (20190447) funded by the Korea Institute of Marine Science & Technology Promotion (KIMST). The authors also would like to thank European Space Agency (ESA) for the distribution of Sentinel-3A and 3B.

References

- Ahn, Y.-H., Moon, J.E., Seo, W.C., Yoon, H.J., 2009. Inherent Optical Properties of Red Tide Algal for Ocean Color Remote Sensing Application. *J. Korean Soc. Mar. Environ. Eng.* 12 (1), 47–54.
- Baban, S.M.J., 1993. Detecting water quality parameters in Norfolk Broads, U.K., using Landsat imagery. *Int. J. Remote Sens.* 14, 1247–1267.
- Bidigare, R.R., Ondrusk, M.E., Morrow, J.H., Kiefer, D.A., 1990. In-vivo absorption properties of algal pigments. *SPIE* 1302, 290–302.
- Brockmann, C., Doerffer, R., Peters, M., Kersttin, S., Embacher, S., Ruescas, A., 2016. Evolution of the C2RCC neural network for Sentinel 2 and 3 for the retrieval of ocean colour products in normal and extreme optically complex waters. In: *Proceedings of the Living Planet Symposium*.
- Cannizzaro, J.P., Carder, K.L., Chen, F.R., Heil, C.A., Vargo, G.A., 2008. A novel technique for detection of the toxic dinoflagellate, *Karenia brevis*, in the Gulf of Mexico from remotely sensed ocean color data. *Cont. Shelf Res.* 28 (1), 137–158.
- Ciotti, A.M., Lewis, M.R., Cullen, J.J., 2002. Assessment of the relationships between dominant cell size in natural phytoplankton communities and the spectral shape of the absorption coefficient. *Limnol. Oceanogr.* 47 (2), 404–417.
- Dierssen, H.M., Kudela, R.M., Ryan, J.P., Zimmerman, R.C., 2006. Red and black tides: Quantitative analysis of water-leaving radiance and perceived color for phytoplankton, colored dissolved organic matter, and suspended sediments. *Limnol. Oceanogr.* 51, 2646–2659.
- Donlon, C., Berruti, B., Buongiorno, A., Ferreira, M.H., Féminias, P., Frerick, J., Goryl, P., Klein, U., Laur, H., Mavrocordatos, C., Nieke, J., Rebhan, H., Seitz, B., Stroede, J., Sciarra, R., 2012. The global monitoring for environment and security (GMES) sentinel-3 mission. *Remote Sens. Environ.* 120, 37–57.
- Elefeldt, M.A., Pasterkamp, R., Woerd, H.J., Pietrzak, J.D., 2008. Remotely sensed seasonality in the spatial distribution of sea-surface suspended particulate matter in the southern North Sea. *Estuarine, Coast. Shelf Sci.* 80 (1), 103–113.
- Feng, C., Ishizaka, J., Saitoh, K., Mine, T., Yamashita, H., 2020. A Novel Method Based on Backscattering for Discriminating Summer Blooms of the Raphidophyte (*Chattonella* spp.) and the Diatom (*Skeletonema* spp.) Using MODIS Images in Ariake Sea. *Japan. Remote Sens.* 12 (9), 1504.
- Ghanea, M., Moradi, M., Kabiri, K., 2016. A novel method for characterizing harmful algal blooms in the Persian Gulf using MODIS measurements. *Advances in Space Res.* 58 (7), 1348–1361.
- Ghatkar, J.G., Singh, R.K., Shanmugam, P., 2019. Classification of algal bloom species from remote sensing data using an extreme gradient boosted decision tree model. *Int. J. Remote Sens.* 40 (24), 9412–9438.
- Gitelson, A., 1992. The peak near 700 nm on radiance spectra of algae and water: relationships of its magnitude and position with chlorophyll concentration. *Int. J. Remote Sens.* 13 (17), 3367–3373.
- Gobler, C., Gobler, C.J., Anderson, O.R., Berry, D.L., Burson, A., Koch, F., Rodgers, B., Koza-Moore, L., Goleski, J., Allam, B., Bowser, P., Tang, Y., Nuzzi, R., 2008. Characterization, dynamics, and ecological impacts of harmful *Cochlodinium* polykrikoides blooms on eastern Long Island, NY, USA. *Harmful Algae* 7, 293–307.
- Gómez, F., Richlen, M.L., Anderson, D.M., 2017. Molecular characterization and morphology of *Cochlodinium strangulatum*, the type species of *Cochlodinium*, and *Margalefidinium* gen. nov. for *C. polykrikoides* and allied species (Gymnodiniales, Dinophyceae). *Harmful Algae* 63, 32–44.
- Gower, J., King, S., Borstad, G., Brown, L., 2005. Detection of intense plankton blooms using the 709 nm band of the MERIS imaging spectrometer. *Int. J. Remote Sens.* 26 (9), 2005–2012.
- Gower, J., King, S., 2007. Validation of chlorophyll fluorescence derived from MERIS on the west coast of Canada. *Int. J. Remote Sens.* 28 (3–4), 625–635.
- Hu, C., Barnes, B.B., Qi, L., Corcoran, A.A., 2015. A harmful algal bloom of *Karenia brevis* in the Northeastern Gulf of Mexico as revealed by MODIS and VIIRS: a comparison. *Sensors* 15 (2), 2873–2887.
- Izadi, M., Sultan, M., Kadiri, R.E., Ghannadi, A., Abdelmohsen, K., 2021. A Remote Sensing and Machine Learning-Based Approach to Forecast the Onset of Harmful Algal Bloom. *Remote Sens.* 13 (19), 3863.
- Jeong, H.J., Kang, C.K., 2013. Understanding and managing red tides in Korea Preface. *Harmful Algae* 30, S1–S2.
- Kim, Y.O., Choi, J., Baek, S.H., Lee, M., Oh, H.M., 2020. Tracking *Alexandrium catenella* from seed-bed to bloom on the southern coast of Korea. *Harmful Algae* 99.
- Kim, S.M., Shin, J., Baek, S., Ryu, J.H., 2019. U-Net convolutional neural network model for deep red tide learning using GOCl. *J. Coast. Res.* 90 (SI), 302–309.
- Kim, Y., Yoo, S., Son, Y.B., 2016. Optical discrimination of harmful *Cochlodinium* polykrikoides blooms in Korean coastal waters. *Opt. Express* 24 (22), A1471–A1488.
- Kohavi, R., 1998. Glossary of terms. *Mach. Learn.* 30, 127–132.
- Lee, C.K., Park, T.G., Park, Y.T., Lim, W.A., 2013. Monitoring and trends in harmful algal blooms and red tides in Korean coastal waters, with emphasis on *Cochlodinium* polykrikoides. *Harmful Algae* 30, S3–S14.
- Lee, M.S., Park, K.A., Chae, J., Park, J.E., Lee, J.S., Lee, J.H., 2020. Red tide detection using deep learning and high-spatial resolution optical satellite imagery. *Int. J. Remote Sens.* 41 (15), 5838–5860.
- Liu, R., Xiao, Y., Ma, Y., Cui, T., An, J., 2022. Red tide detection based on high spatial resolution broad band optical satellite data. *ISPRS J. Photogramm. Remote Sens.* 184, 131–147.
- Lou, X., Hu, C., 2014. Diurnal changes of a harmful algal bloom in the East China Sea: Observations from GOCl. *Remote Sens. Environ.* 140, 562–572.
- Matsuoka, K., Fukuyo, Y., 2003. Taxonomy of cysts. *Manual on Harmful Marine Microalgae*. UNESCO, Paris, pp. 563–592.
- Miller, R.L., McKee, B.A., 2004. Using MODIS Terra 250 m imagery to map concentration of total suspended matter in coastal waters. *Remote Sens. Environ.* 93, 259–266.
- Murphy, K.P., 2012. *Machine learning: a probabilistic perspective*. MIT press, p. 245p.
- Nair, A., Sathyendranath, S., Platt, T., Morales, J., Stuart, V., Forget, M. H., Devred, E., Bouman, H., 2008. Remote sensing of phytoplankton functional types. *Remote Sens. Environ.* 112(8), 3366–3375.
- National Institute of Fisheries Science (NIFS). Harmful Algal Blooms in Korean Coastal Waters; National Institute of Fisheries Science: Busan, Korea, 2015.
- Noh, J.H., Kim, W., Son, S.H., Ahn, J.H., Park, Y.J., 2018. Remote quantification of *Cochlodinium polykrikoides* blooms occurring in the East Sea using geostationary ocean color imager (GOCl). *Harmful algae* 73, 129–137.
- Park, T.G., Lim, W.A., Park, Y.T., Lee, C.K., Jeong, H.J., 2013. Economic impact, management and mitigation of red tides in Korea. *Harmful Algae* 30 (Suppl. 1), S131–S143.
- Qi, L., Hu, C., Cannizzaro, J., Corcoran, A.A., English, D., Le, C., 2015. VIIRS observations of a *Karenia brevis* bloom in the Northeastern Gulf of Mexico in the absence of a fluorescence band. *IEEE Geosci. Remote Sens. Lett.* 12 (11), 2213–2217.
- Rodríguez-Benito, C.V., Navarro, G., Caballero, I., 2020. Using Copernicus Sentinel-2 and Sentinel-3 data to monitor harmful algal blooms in Southern Chile during the COVID-19 lockdown. *Mar. Pollut. Bull.* 161.
- Ryan, J.P., Fischer, A.M., Kudela, R.M., Gower, J.F., King, S.A., Marin, I.I.R., Chavez, F. P., 2009. Influences of upwelling and downwelling winds on red tide bloom dynamics in Monterey Bay, California. *Cont. Shelf Res.* 29 (5–6), 785–795.
- Sathyendranath, S., Watts, L., Devred, E., Platt, T., Caverhill, C., Maass, H., 2004. Discrimination of diatoms from other phytoplankton using ocean-colour data. *Mar. Ecol. Prog. Ser.* 272, 59–68.
- Schalles, J.F., 2006. Optical remote sensing techniques to estimate phytoplankton chlorophyll a concentrations in coastal waters with varying suspended matter and CDOM concentrations. In: *Remote Sensing and Digital Image Processing*; Springer International: Dordrecht, The Netherlands, 2006; Volume 9, pp. 27–79.
- Shang, S., Wu, J., Huang, B., Lin, G., Lee, Z., Liu, J., Shang, S., 2014. A new approach to discriminate dinoflagellate from diatom blooms from space in the East China Sea. *J. Geophys. Res. Ocean.* 119 (7), 4653–4668.
- Shin, J., Kim, S.M., Son, Y.B., Kim, K., Ryu, J.H., 2019. Early prediction of *Margalefidinium polykrikoides* bloom using a LSTM neural network model in the South Sea of Korea. *J. Coast. Res.* 90 (SI), 236–242.
- Shin, J., Kim, K., Son, Y.B., Ryu, J.H., 2019. Synergistic effect of multi-sensor Data on the detection of *Margalefidinium polykrikoides* in the South Sea of Korea. *Remote Sens.* 11 (1), 36.
- Shin, J., Jo, Y.H., Ryu, J.H., Khim, B.K., Kim, S.M., 2021. High Spatial-Resolution Red Tide Detection in the Southern Coast of Korea Using U-Net from PlanetScope Imagery. *Sensors* 21 (13), 4447.
- Shin, J.S., Min, J.E., Ryu, J.H., 2017. A study on red tide surveillance system around the Korean coastal waters using GOCl. *Korean J. Remote Sens.* 33, 213–230.
- Son, Y.B., Kang, Y.H., Ryu, J.H., Jeong, J.C., 2012. Satellite detection of harmful algal bloom occurrences in Korean waters. *Korean J. Remote Sens.* 28, 531–548.
- Suh, Y.S., Jang, L.H., Lee, N.K., Ishizaka, J., 2004. Feasibility of red tide detection around Korean waters using satellite remote sensing. *Fisher Aqua. Sci.* 7, 148–162.
- Tang, Y.Z., Gobler, C.J., 2009. Characterization of the toxicity of *Cochlodinium* polykrikoides isolates from Northeast US estuaries to finfish and shellfish. *Harmful Algae* 8, 454–464.
- Tao, B., Mao, Z., Lei, H., Pan, D., Shen, Y., Bai, Y., Zhu, Q., Li, Z., 2015. A novel method for discriminating *Prorocentrum donghaiense* from diatom blooms in the East China Sea using MODIS measurements. *Remote Sens. Environ.* 158, 267–280.
- Tekerék, A., Yapıcı, M.M., 2022. A novel malware classification and augmentation model based on convolutional neural network. *Comput. Secur.* 112.
- Tomlinson, M.C., Stumpf, R.P., Ransibrahmanakul, V., Truby, E.W., Kirkpatrick, G.J., Pederson, B.A., Gabriel, A.V., Heil, C.A., 2004. Evaluation of the use of SeaWiFS imagery for detecting *Karenia brevis* harmful algal blooms in the eastern Gulf of Mexico. *Remote Sens. Environ.* 91, 293–303.
- Tomlinson, M.C., Wynne, T.T., Stumpf, R.P., 2009. An evaluation of remote sensing techniques for enhanced detection of the toxic dinoflagellate *Karenia brevis*. *Remote Sens. Environ.* 113, 598–609.
- Westberry, T.K., Siegel, D.A., Subramaniam, A., 2005. An improved bio-optical model for the remote sensing of *Trichodesmium* spp. blooms. *J. Geophys. Res. Ocean.* 110, 1–11.
- Whyte, J.N.C., Haigh, N., Ginther, N.G., Keddy, L.J., 2001. First record of blooms of *Cochlodinium* sp. (Gymnodiniales, Dinophyceae) causing mortality to aquacultured salmon on the west coast of Canada. *Phycol.* 40 (3), 298–304.
- Yamashita, R., Nishio, M., Do, R.K.G., Togashi, K., 2018. Convolutional neural networks: an overview and application in radiology. *Insights Imag.* 9 (4), 611–629.
- Yoon, H.J., Nam, K.W., Cho, H.G., Beun, H.K., 2004. Study on monitoring and prediction for the red tide occurrence in the middle coastal area in the South Sea of Korea II. The relationship between the red tide occurrence and the oceanographic factors. *J. Korea Inst. Inf. Commun. Eng.* 8 (4), 938–945.
- Zhao, J., Temimi, M., Ghedira, H., 2015. Characterization of harmful algal blooms (HABs) in the Arabian Gulf and the Sea of Oman using MERIS fluorescence data. *ISPRS J. Photogramm. Remote Sens.* 101, 125–136.